Chapter 7
Interface Reactions Between the Metal Melt and the Filter Surface Activated by a Spark Plasma Sintering Process

Anton Salomon, Mykhaylo Motylenko, Martin Thümmler, and David Rafaja

7.1 Introduction

The understanding of the interface reactions between metal melts containing inclusions and the filter ceramic surfaces is essential for the development of functional materials for active and reactive filtration of metallic melts. On the laboratory scale, the filtration processes and the deposition of inclusions in ceramic filters are typically analyzed using impingement trials [1–3] or casting simulators [4], before the filters are subjected to prototype casting on industrial scale [5]. However, the results of such experiments are sometimes hardly to interpret. The main reason is that these experiments activate several simultaneous processes, which involve heterogeneous reactions between the metallic melt and the surface of the functional ceramics, production of inclusions in the melt and their deposition on the surface of the functional ceramics, and finally the solid state reactions and diffusion processes between the products of the heterogeneous reactions and the functionalized filter material. Furthermore, these processes are superimposed by the melt flow and/or by the macroscopic convection. Although the traditional laboratory experiments reveal important information about the thermal shock behavior [1, 6], melt flow rate [5, 7] and filtration efficiency [5, 7, 8] of the filters, which is usually complemented by the amount and chemical composition of the deposited non-metallic inclusions, they cannot substitute an in-depth investigation of the fundamental mechanisms of the interface and bulk reactions, which is required for a targeted development of the metal melt filters.

This chapter illustrates how the Spark Plasma Sintering (SPS) can be employed as a generally applicable but more controlled method to produce interface and reaction layers between metal melts and filter ceramics for advanced analysis

A. Salomon · M. Motylenko · M. Thümmler · D. Rafaja (✉)
Institute of Materials Science, Technische Universität Bergakademie Freiberg,
Gustav-Zeuner-Straße 5, 09599 Freiberg, Germany
e-mail: rafaja@iww.tu-freiberg.de

C. G. Aneziris and H. Biermann (eds.), *Multifunctional Ceramic Filter Systems for Metal Melt Filtration*, Springer Series in Materials Science 337,
https://doi.org/10.1007/978-3-031-40930-1_7

of filtration processes. The SPS technology, which was originally developed for powder compaction and sintering [9], offers a high variability of process parameters, controlled heating and cooling rates, and widely adjustable dwell temperatures, holding times and atmospheres. In this work, SPS was utilized to melt the 42CrMo4 steel, aluminum and AlSi7Mg alloy that were in a direct contact with selected refractories like alumina, mullite, silicon oxide, titanium oxide, carbon-bonded alumina and carbon-bonded magnesia.

In contrast to other techniques, which bring molten metals in contact with the functionalized metal melt filters, the metal melting in a SPS apparatus minimizes the macroscopic melt flow, which is usually responsible for damage or even for removal of the newly formed reaction products and layers from the filter surface. Furthermore, the SPS allows working with extremely variable sample geometry including planar metal-ceramic interfaces in combination with bulk filter materials up to the powder mixtures of metal and ceramics with a huge contact area between the counterparts, with short reaction diffusion paths and with the finite geometry of the diffusion couples. The samples with planar geometry were utilized to analyze the sequence and morphology of new phases formed at the metal-ceramic interface. The experiments done on powder mixtures assisted in the identification and description of phases with narrow homogeneity ranges, and produced equilibrium-state samples for comparison with the thermodynamic calculations. Thus, the SPS-based melting technique provides complementary results with respect to the classical casting experiments or impingement tests, and helps to elucidate the reaction steps, which are frequently inaccessible, when the established methods are used.

7.2 Adaptation of the Spark Plasma Sintering for Metal Melting

The Spark Plasma Sintering or Field Assisted Sintering Technology (SPS/FAST) is based on resistive Joule heating through the pulsed electric direct current (DC) that passes electrically conducting graphite tools and/or the sample, if the sample is electrically conducting as well [9]. The Joule heating by the graphite die or directly by the sample itself allows for high heating rates. The typical current used for SPS/FAST is in the kA range. For sample having a diameter of about 2 cm, this current corresponds to the current density of approx. 1 kA/cm^2. Although the voltage on the sample is relatively low (max. 10 V), the heating power is still about 30 kW. The sintering atmosphere is usually vacuum or some inert gas like nitrogen or argon [9]. As the SPS/FAST process was developed mainly for compacting and short time sintering of refractories, the standard SPS/FAST tools are not constructed for an extensive melting of one of the components. During the fast melting experiments, however, the metal has to be molten. Therefore, new sample environments must be developed for such experiments, because the molten metal would leak from the sample environment and react quickly with the carbon present in the graphite tools.

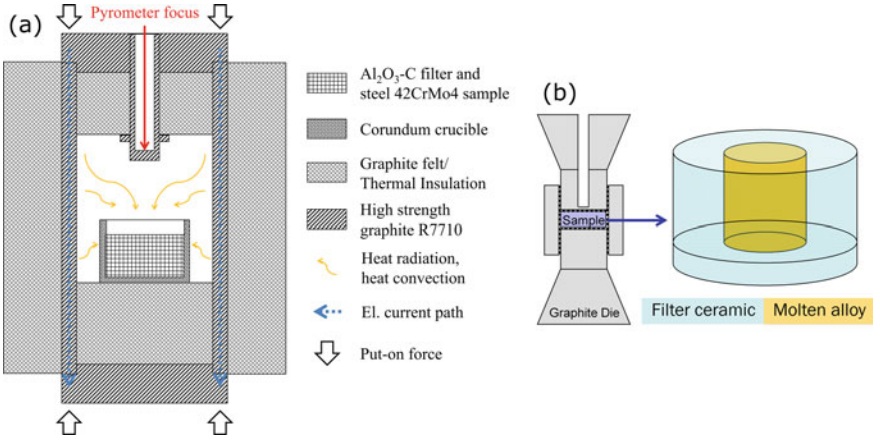

Fig. 7.1 Scheme of the high-speed furnace **a** and tool-in-tool setup **b** used for the sample production ((**b**) adopted from [11])

The first development is a corundum crucible, which is filled with the functionalized filter material and with the metal powder to be molten. The crucible itself is located in a tube made of high strength graphite, which serves as a heater (Fig. 7.1a). The outer diameter of the tube is about 100 mm, the thickness of the walls about 10 mm [10]. In this "high speed furnace", the samples are heated indirectly by the heat irradiated from the heater and by the heat convection. Because of the indirect heating, the heating rate is below 200 K min^{-1}, significantly faster than in a conventional furnace but slower than usual SPS. Still, this tool is useful for special experiments with large samples that should be kept at the dwell temperature for long holding times, for instance during the investigation of the metal infiltration into the real filter structures. A drawback of this tool is the expected inaccuracy of the temperature measurement by a pyrometer, which is focused to a graphite finger that is not in a direct contact with the sample under study.

The second sample environment is based on a "tool-in-tool" setup [11], in which the metal powder to be molten is placed within a crucible that is made from or coated by the functionalized filter ceramics. The ceramic parts were cut from suspension nozzles or produced by slip casting according to the procedures presented in references [1, 2, 7, 8, 12–14]. The size of the ceramic crucible was usually 20 mm in diameter with an internal cavity of 5 to 10 mm. The whole inserts were located at the position, which corresponds to the sample position in a standard SPS experiment (Fig. 7.1b). Due to the small size of the inserts and the direct contact between the heater and the sample, very high heating rates up to 1500 K min^{-1} were achieved [3]. As this setup offered much higher heating rates and an easier handling than the previous one, it was used for the majority of the SPS experiments.

7.3 Methods of Structure and Microstructure Analysis

On the microscopic scale, the solidified products of the chemical reactions between the molten metals and the surface of the ceramic filter were analyzed using scanning electron microscopy with energy dispersive X-ray spectroscopy (SEM/EDX) and electron backscatter diffraction (SEM/EBSD). The elemental analysis using SEM/EDX was complemented by the electron probe microanalysis with wavelength dispersive X-ray spectroscopy (EPMA/WDX). For SEM/EDX/EBSD, a high-resolution SEM LEO-1530 (Carl Zeiss AG, Germany) with field-emission cathode, an EDX detector (Bruker AXS) and a Nordlys II EBSD detector (HKL Technology) was used. The SEM imaging was performed using secondary electrons, back-scattered electrons or in a combined mode. The SEM/EDX/EBSD experiments were carried out at an acceleration voltage of 20 kV. The working distance for EBSD was 15 mm, the tilting angle of the sample 70° and the step size 0.3 μm. For identification of the Kikuchi patterns and for the evaluation of the measured data, the software package Channel 5 (HKL Technology) was used. For the EPMA/WDX measurements, an electron probe microanalyzer JXA-8230 SuperProbe (Jeol GmbH, Germany) with five-crystal spectrometers was used. The EPMA scans were performed with the step size of 0.5 μm.

The phase compositions of the solidified samples were analyzed using a Bragg–Brentano diffractometer URD 63 (Freiberger Praezisionsmechanik) that was equipped with a sealed X-ray tube with copper anode and with a curved graphite monochromator located in front of a scintillation detector. The X-ray diffraction (XRD) patterns patterns were collected between $2\theta = 20°$ and 150° with the step size of $\Delta 2\theta = 0.04°$, and with the counting time of 10 s per step. The phase composition of the samples was quantified by using the Rietveld method [15, 16] implemented in the computer program MAUD [17].

On the nanoscale, the samples were characterized using transmission electron microscopy (TEM), selected area electron diffraction (SAED) and energy dispersive X-ray spectroscopy (EDX/TEM). These analyses were done in a JEM 2200 FS transmission electron microscope (JEOL Ltd., Japan) at an acceleration voltage of 200 kV. The TEM samples were prepared by the focused ion beam method (FIB) with a Helios NanoLab 600i (FEI, USA) in form of thin slices.

7.3.1 Reactions Between Molten Steel and Corundum-Based Refractories with Different Carbon Contents

In analogy to the established entry nozzles [18–21], the newly developed carbon-bonded alumina (Al_2O_3-C) filters [8, 13, 14] are expected to react with molten steels and to form new interface layers between the metallic melt and the filter surface. Already the formation of the interface layer should significantly contribute to the removal of unwanted oxygen or other contaminating elements [10]. The interface

Table 7.1 Chemical composition of the utilized steel alloy 42CrMo4 as provided by the powder vender

Element	C	Cr	Mo	Si	Mn	Fe
Mass%	0.4	1.0	0.2	0.2	0.7	Balance

layer itself has to attract and to embed non-metallic inclusions. Generally, the chemical composition and the phase composition of the layer are considered as crucial factors influencing the agglomeration of non-metallic inclusions and their adherence to the filter surface [7, 22]. The carbon additions should improve the high-temperature mechanical properties of the alumina filters [23–26], their thermal shock resistance (via higher thermal conductivity and low thermal expansion) [8, 25] and their resistance against crack initiation and propagation [26]. In this section, the formation of a secondary alumina layer at the interface between the Al_2O_3-C filters with different carbon contents and molten steel 42CrMo4 is described. The chemical composition of the steel is summarized in Table 7.1. The reaction experiments presented here were performed using the tool-in-tool setup with the respective carbon-containing alumina ceramic acting as the reaction vessel.

7.3.2 Time-Dependent Layer Growth and Reaction Scheme on the Microscopic Level

According to the thermodynamic model proposed by Zienert et al. [27], Al_2O_3 is partially decomposed by liquid iron. The decomposition of alumina is facilitated by the presence of carbon in the reaction zone, which also reacts with dissolved oxygen to CO and/or CO_2 [27, 28]. The CO/CO_2 gas leaves partially the reaction zone. The formation and evaporation of CO/CO_2 decreases the carbon concentration in the reaction zone and decelerates the decomposition of Al_2O_3. Nevertheless, if sufficient amount of carbon is present in the filter material, alumina is permanently dissolved in the liquid iron [27–29], which leads to an increase of the concentration of aluminum in the melt.

The microstructural consequences of a short-time reaction between the carbon binder and the dissolved oxygen stemming from the decomposed alumina are illustrated in Fig. 7.2. The contact region between the solidified steel and Al_2O_3(-C) becomes carbon deficient or even carbon-free. The thickness of the carbon-depleted zone does not exceed 40 – 50 μm and is almost independent of the dwell time. Liquid iron, which contributes substantially to the decomposition of alumina, can be observed in form of solidified droplets in the filter constituents containing simultaneously alumina and carbon. In the functional filter coating containing no carbon (Fig. 7.2a), the solidified droplets were observed only in the carbon-bonded alumina filter struts. In the functionalized filter coatings containing carbon (Fig. 7.2b and c), the solidified droplets were observed already in the functional coating. Increased

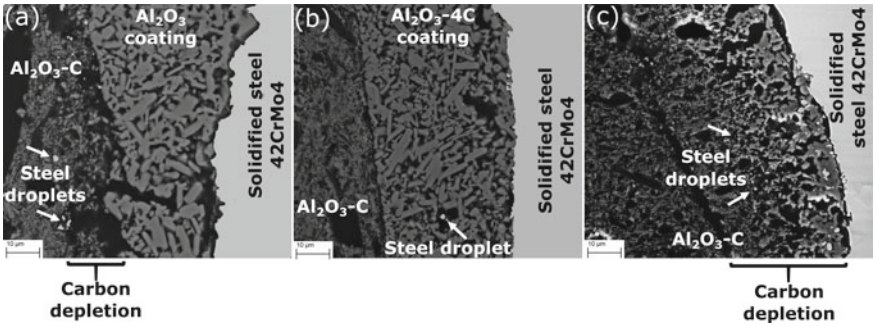

Fig. 7.2 SEM micrographs (BSE contrast) of functionalized Al_2O_3-C filters that were exposed to molten steel 42CrMo4 in the SPS apparatus at 1600 °C for 1 min. The functional coatings consist of corundum without carbon (**a**), Al_2O_3-C with 4 mass% C (**b**), and Al_2O_3-C with 30 mass% C (**c**) (adopted from [29])

concentrations of Al and O in the solidified steel melt were revealed by the SEM/EDS measurements [11, 29]. Figure 7.3a shows the grooves stemming from the escape of the CO/CO_2 bubbles, which were formed during the reaction of free oxygen with the carbon binder. The escape of the CO/CO_2 bubbles is the main reason for the decarburization of the C-bonded Al_2O_3 filter ceramic.

The results of these experiments confirmed that the local concentration of carbon is a crucial factor influencing the rate of the concurrent reactions, namely alumina dissolution and the formation of secondary corundum. Although these reactions occur in contact with liquid iron, the dissolution of Al_2O_3 is facilitated by the presence of carbon, which reacts with free oxygen, while the formation of secondary corundum is assisted by the absence of carbon. For this reason, secondary corundum forms preferentially at the filter surface, i.e., in the carbon-depleted zone, where a sufficiently

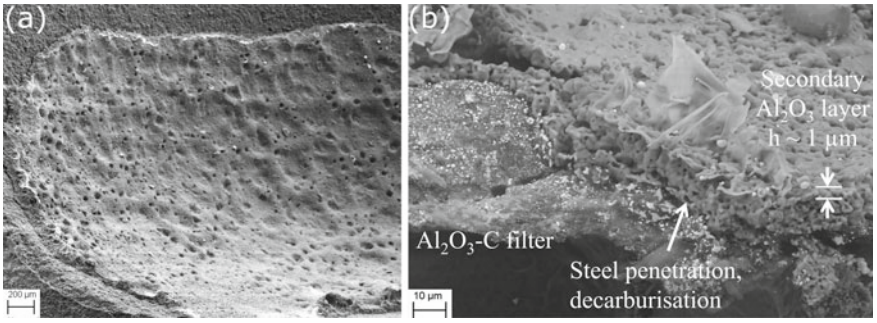

Fig. 7.3 SEM micrographs (SE contrast) of the surface of Al_2O_3-C with 30 mass% of C after SPS at 1600 °C: Layer formed on top of the ceramic body after 1 min with grooves stemming from the escape of CO/CO_2 bubbles (**a**); penetration of the steel melt into the filter, decarburization of Al_2O_3-C and formation of a secondary Al_2O_3 layer with a thickness below 1 µm after 10 min (**b**) ((**a**) adopted from [11])

high amount of dissolved aluminum and oxygen is present (Fig. 7.3b) [27, 29]. The formation of secondary corundum was observed mainly in samples that were kept at high temperature for a longer time (Fig. 7.4). Besides the dwell time, the rate of the CO/CO_2 gas formation is another important factor controlling the secondary corundum formation, because it affects the local concentration of carbon in the filter ceramics.

Also the morphology of the Al_2O_3(-C) filters, their porosity, and the morphology of secondary corundum are additional important factors influencing both reaction processes [27, 29]. At a sufficiently high local concentration of carbon, the secondarily formed corundum can be reduced like the primary corundum in the filter, if it forms only small and separated crystallites that can be soaked by liquid iron containing carbon from the binder [27, 29]. On the other hand, compact and large grains of secondary corundum, which are in contact with carbon-depleted steel melt (Fig. 7.4a-c), stay stable. Hence, the formation of a dense, impenetrable layer of secondary corundum provides an efficient barrier for carbon diffusion from the Al_2O_3-C filter and iron penetration into the filter, and thus inhibits the decomposition of Al_2O_3 [29]. Still, the reaction layer serves as a docking site for non-metallic inclusions contained in the melt (Fig. 7.5).

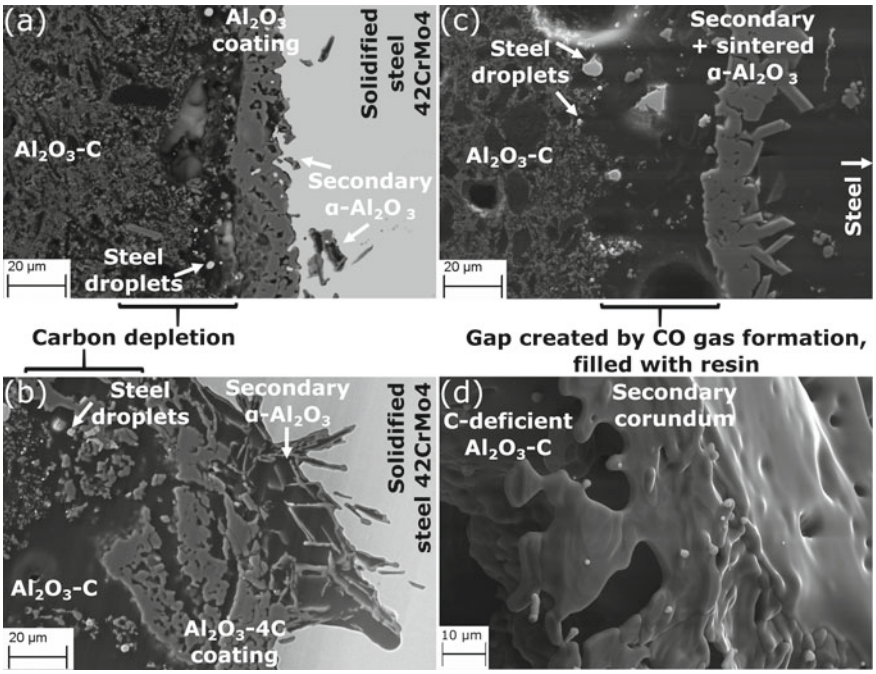

Fig. 7.4 SEM micrographs (SE contrast) of functionalized Al_2O_3-C filters that were exposed to molten steel 42CrMo4 in SPS apparatus at 1600 °C for **a**–**c** 30 min and **d** for 5 min. The functional coatings consist of **a** corundum without carbon, **b** Al_2O_3-C with 4 mass% C, and **c**, **d** Al_2O_3-C with 30 mass% C (adopted from [29])

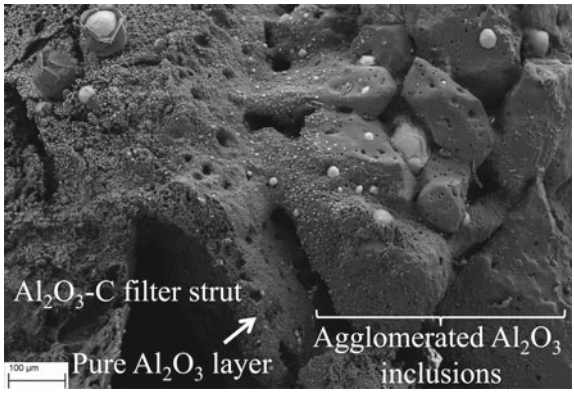

Fig. 7.5 SEM micrograph (BSE/SE) of agglomerated Al_2O_3 inclusions deposited on the Al_2O_3-C filter after 5 min at 1600 °C. The secondary Al_2O_3 layer "bridges" between the agglomerate and the filter

The majority of the inclusions consisted of aluminum oxides. Other endogenous inclusions contained MnS (SG $Fm\bar{3}m$) [11]. According to Sims and Dahle [30], the MnS precipitates can be classified as type II and III. They were found at the high-angle grain boundaries, free surface of the steel droplets and at the interfaces formed between the ceramics and the steel. In addition, MnS in form of a thin film covered partly the Al_2O_3 inclusions (Fig. 7.6). The formation of the MnS film was explained by the heterogeneous nucleation of the sulfide on oxide surfaces and by the supersaturation of Mn and S in the areas of final solidification [31]. Unfortunately, the described MnS formation on inclusion surfaces results in so-called duplex inclusions that are detrimental for the mechanical properties of any (cast) metallic part [32].

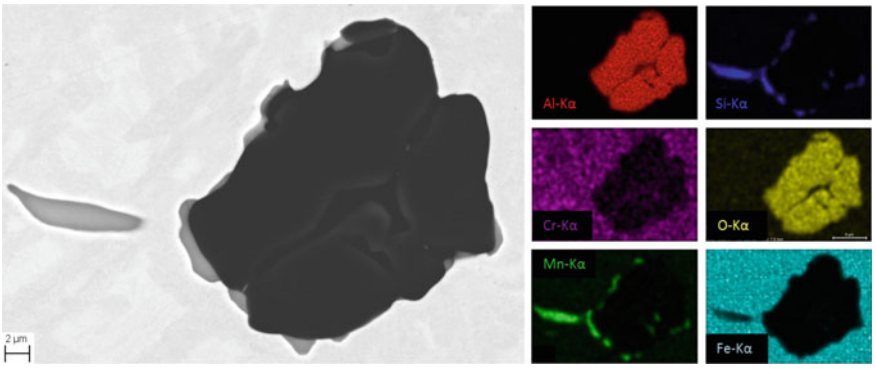

Fig. 7.6 SEM micrograph (BSE contrast) of an Al_2O_3 particle within solidified 42CrMo4 steel (bright gray) partly covered with MnS (dark gray) after 1 min at 1600 °C, and EDX element distribution maps on the right (adopted from [11])

7.3.3 *Interface Reactions Preceding the Secondary Corundum Formation*

High efficiency of the filtration processes requires a good adhesion of the non-metallic inclusions and/or reaction products to the functionalized filter surface in order to inhibit their spalling and the contamination of the metallic melt. It is assumed that materials having the same chemical composition or similar crystal structures possess better adhesion than fully incompatible compounds. As the secondary corundum grows on the filter surface that contains primary corundum, a local epitaxial growth was considered. However, the SEM/EBSD measurements, which were carried out on the metal melt filter covered by a functional Al_2O_3-C coating with 4 mass% C, revealed that the secondary corundum grows in form of interconnected, almost single-crystalline platelets, but without any pronounced orientation relationship to the corundum substrate (Fig. 7.7). This result motivated further studies, which should elucidate the early stages of the chemical reactions at the interface between the functionalized filter surface and the metallic melt that precede the growth of secondary corundum. These studies were carried out on functional Al_2O_3 coatings containing no carbon, 4 mass% C or 30 mass% C that were treated for a short time (1 – 2 min) at 1600 °C in the SPS apparatus or in a steel-casting simulator. The chemical composition of the interface layers was analyzed using EDX in TEM. The phase composition of the interlayers was concluded from the SAED patterns.

The chemical analysis of the interlayers using EDX confirmed the presence of iron, aluminum and oxygen, which are involved in the carbothermic reaction, as well as the presence of the alloying elements from the steel, mainly silicon [13, 29]. The SAED analysis revealed that the interlayers are almost amorphous (Figs. 7.8 and 7.9). Still, the contrasts observed in the TEM micrographs indicated fluctuations in the chemical and possibly in the phase composition, including the presence of nanocrystalline phases. Detailed analysis of the SAED patterns (Fig. 7.10) disclosed that the nanocrystalline phases contain wuestite (FeO, SG $Fm\bar{3}m$), spinel-like phases with the chemical composition $A^{2+}B_2^{3+}O_4^{2-}$ (A and B being Fe, Al, Si and/or Mg contaminant) and the space group $Fd\bar{3}m$ and garnet-like structures, most probably $Fe_3Al_2(SiO_4)_3$ (SG $Ia\bar{3}d$) [29]. After longer reaction times of a few minutes, the nanocrystalline oxide phases are replaced by corundum. A possible transient phase is metastable γ-Al_2O_3, which possesses a spinel-like crystal structure (SG $Fd\bar{3}m$) containing highly mobile structural vacancies [33]. The structural vacancies facilitate the necessary fast exchange of metallic (cationic) species to remove iron and/or silicon from the spinel-like structure of $A^{2+}B_2^{3+}O_4^{2-}$.

When the seeds of secondary corundum in the interlayer are in a direct contact with the primary corundum from the functionalized coating, the secondary corundum grows epitaxially on the primary corundum (regions 1 and 2 in Fig. 7.11). Platelets of the secondary corundum, which grow from aluminum and oxygen dissolved in the steel melt on the amorphous interlayer, do not develop any pronounced orientation relationship to the filter surface (region 3 in Fig. 7.11), because the amorphous interlayer inhibits the epitaxial growth. Whereas the amorphous layers form on the surface

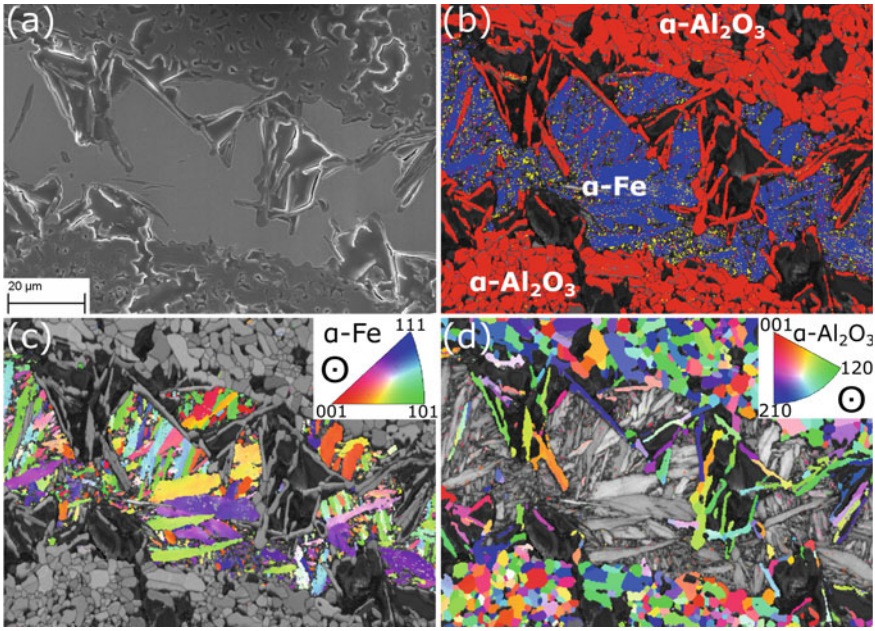

Fig. 7.7 **a** SEM micrograph (SE contrast) of the interface between the solidified steel 42CrMo4 and the functional Al_2O_3-C coating with 4 mass% C after the reaction for 30 min at 1600 °C. **b** Phase map, **c** local orientations of the grains, and **d** local orientations of corundum. Yellow spots in panel (**b**) are MnS inclusions with an fcc crystal structure. The orientation distribution maps in panels (**c**) and (**d**) are related to the direction perpendicular to the image plane (adopted from [29])

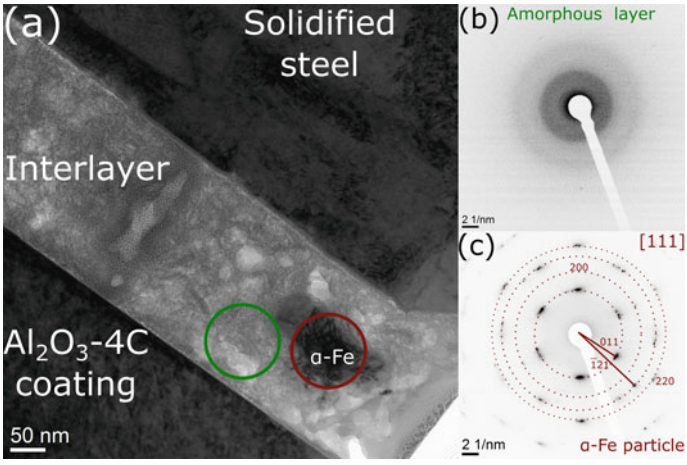

Fig. 7.8 **a** TEM micrograph of an interlayer formed between solidified steel 42CrMo4 and an α-Al_2O_3 coating with 4 mass% C. The reaction experiment was conducted in SPS apparatus at the dwell time of 1 min at 1600 °C. **b** SAED pattern of the interface layer. **c** SAED of an α-Fe particle embedded in the amorphous layer (adopted from [29])

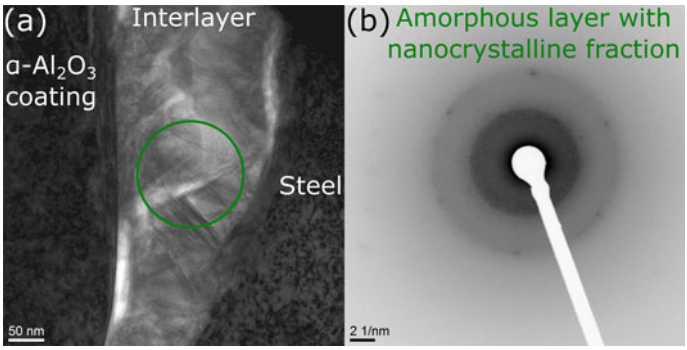

Fig. 7.9 **a** TEM micrograph of an interface layer formed between solidified steel 42CrMo4 and a carbon-free functional corundum coating. The reaction experiment was conducted in a steel-casting simulator. The immersion time was 2 min at 1600 °C. **b** SAED pattern of the interface layer (adopted from [29])

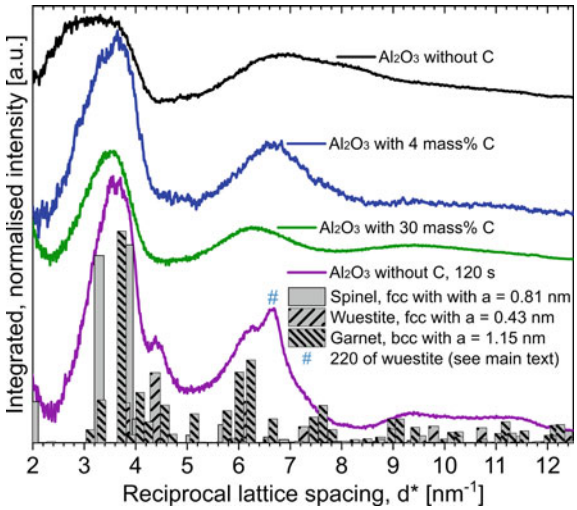

Fig. 7.10 Diffracted intensities obtained by integrating the SAED patterns of the observed Fe–O-(Al-Si)-containing interlayers in the azimuthal direction and plotted versus the reciprocal lattice spacing, calculated according to $d^* = 1/d = \sqrt{h^2 + k^2 + l^2}/a$ for the respective lattice parameter a and the diffraction indices hkl. Theoretical peak positions and the diffracted intensities are shown in a bar chart with differently shaded bars at the bottom of the figure for a spinel structure with a lattice parameter of about 0.81 nm, for fcc wuestite with a lattice parameter of about 0.43 nm and a garnet phase with a lattice parameter of about 1.15 nm. The diffracted intensities were calculated using kinematical diffraction theory assuming random orientation of crystallites (adopted from [29])

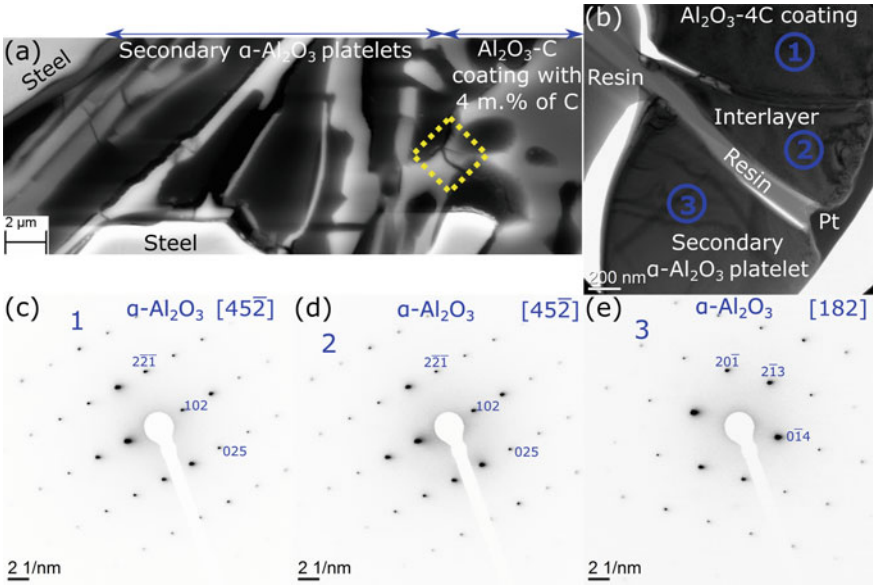

Fig. 7.11 **a** SEM micrograph of a transition region between the Al_2O_3-C functional coating containing 4 mass% C and the α-Al_2O_3 platelets showing the position of the FIB sample (highlighted area). The reaction time was 30 min at 1600 °C. **b** TEM micrograph showing an Al_2O_3 interlayer grown on the surface of the functional coatings and an Al_2O_3 platelet. The corresponding SAED patterns are displayed in panels (**c**)–(**e**) (adopted from [29])

of all Al_2O_3-C filters independently of their carbon content, the secondary corundum possesses different morphologies, which depend on the local carbon supply and thus on growth kinetics [29], as discussed in the previous section.

7.4 Reactions Between Molten Steel and Carbon-Bonded Corundum Coated with Carbon-Bonded Magnesia

Carbon-bonded magnesia (MgO-C) combines low thermal expansion and high thermal conductivity of the graphite binder with a low wettability of the composite against slags and metal melts [34]. In analogy to Al_2O_3-C (cf. previous sections), MgO in MgO-C is decomposed and CO/CO_2 gas is formed, when the refractory is brought in contact with liquid steel [14, 27, 34–37]. Dissolved magnesium and oxygen form secondary MgO, which deposits as a dense, thin layer at the steel/refractory interface [36, 38, 39], analogously to the formation of secondary Al_2O_3. After a longer reaction time, $MgAl_2O_4$ whisker-like fibers (SG $Fd\bar{3}m$) formed at the interface between the MgO-C coating and the Al_2O_3-C filter substrate (Fig. 7.12). The fibers grow during a vapor–liquid-solid process [4, 37]. The reactants are Mg,

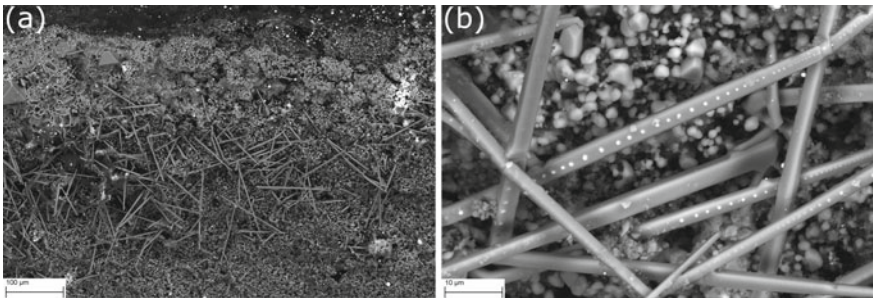

Fig. 7.12 SEM micrograph (BSE) of the contact area between MgO-C coating and Al_2O_3-C substrate ceramic after 60 min at 1600 °C. **a** Fibre formation observed in the contact area; **b** enlarged cut-out of (**a**) showing iron incorporation (bright spheres) within the fibres (adopted from [37])

Al and O that are dissolved in the liquid steel penetrating the porous MgO-C coating [40].

In addition to $MgAl_2O_4$ whiskers, a dense layer of $MgAl_2O_4$ formed at the former MgO-C/steel interface (Fig. 7.13a) [4, 37]. The Al enrichment on the edges of the pre-existing MgO grains of the MgO-C coating produced MgO/$MgAl_2O_4$ core/rim structures within the filter ceramic coating [37]. Vice versa, $MgAl_2O_4$ formed also on the edges or rims of exogenous Al_2O_3 inclusions that were present in the steel (Fig. 7.13b).

The SPS/FAST experiments helped to confirm the assumed "reactive" behavior of the carbon-bonded magnesia coatings deposited on the carbon-bonded alumina filter substrates. The $MgAl_2O_4$ formation on the filter surface and on exogenous inclusions was accompanied by a reduction of the oxygen concentration in the steel. The dense layer of $MgAl_2O_4$ is expected to represent a limiting factor for a further penetration of the molten steel into the interior of the filter material. Thus, a compact $MgAl_2O_4$ layer will slow down the reaction kinetics in analogy with a compact Al_2O_3 coating discussed above. In contrast, the $MgAl_2O_4$ whiskers act against the shrinkage of the

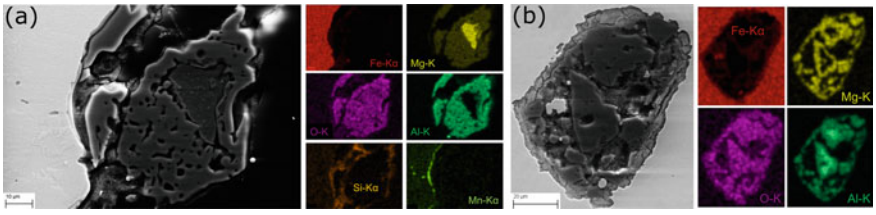

Fig. 7.13 **a** SEM micrograph (BSE) of the steel/MgO-C interface (crosscut) after 60 min at 1600 °C with corresponding EDX elemental mapping. $MgAl_2O_4$ formation on the rim of an MgO grain, Fe–Si–O-rich (fayalite) formation and MnS collection (only Mn shown) is indicated. **b** SEM micrograph (SE contrast) of an Al_2O_3 cluster found within the 42CrMo4 steel after 1 min at 1600 °C and corresponding EDX elemental maps (adopted from [37])

filter during the filtration process [6] and could also be used to increase the strength of the functionalized filter ceramic [4, 37, 40].

7.4.1 Reactions Between Molten Aluminum or AlSi7Mg0.6 Alloy and Selected Carbon-Free Oxide Coatings

Corundum foam filters are used as a standard tool for the aluminum melt filtration [2]. Still, alternative functional materials with specific wettability [41], selective reactivity and interactivity with respect to certain impurities and inclusions are sought. This contribution focusses on mullite ($3Al_2O_3{\cdot}2SiO_2$, SG *Pbam*), amorphous SiO_2 and rutile (TiO_2, SG $P4_2/mnm$), which are considered for production of functional coatings. The main phenomena under study were the reaction of the functional coatings with molten aluminum and molten AlSi7Mg0.6 alloy, formation of the reaction layers on the filter surface and the mechanisms of the adhesion between the reaction layers and the functionalized filter surface. Chemical composition of the AlSi7Mg0.6 alloy is presented in Table 7.2. The majority of the experiments discussed in this subchapter were performed in the SPS apparatus using the tool-in-tool setup. Additional experiments were done via impingement tests [1–3] and sessile drop experiments [41]. The temperature of the melt was always 750 °C.

7.4.2 Reaction Between AlSi7Mg0.6 and Corundum

For short dwell time (1 min), no reaction layers were detected on the surface of the corundum filters. The results of the SPS treatment and the impingement tests were identical, as for both methods the liquid AlSiMg0.6 did not penetrate into the almost dense ceramics. For the SPS-treated samples, slightly better wetting of the corundum filter by the molten aluminum alloy was observed. This phenomenon was attributed to the destruction of the thin oxide layer formed on the surface of original AlSi7Mg0.6 particles in the SPS melting process. The oxide layer is disrupted through the percolation of the electric current and removed by the reducing conditions in the SPS process, which are established by the application of the graphite tooling [3].

Table 7.2 Chemical composition of the aluminum alloy powder used for the melt production as specified by the manufacturer

Alloy	Elemental composition [mass%]							Particle size	Source
	Al	Si	Mg	Fe	Cu	Mn	Zn		
AlSi7Mg0.6	Balance	7.07	0.61	0.09	0.09	0.02	0.28	45 – 100 µm	TLS Technik

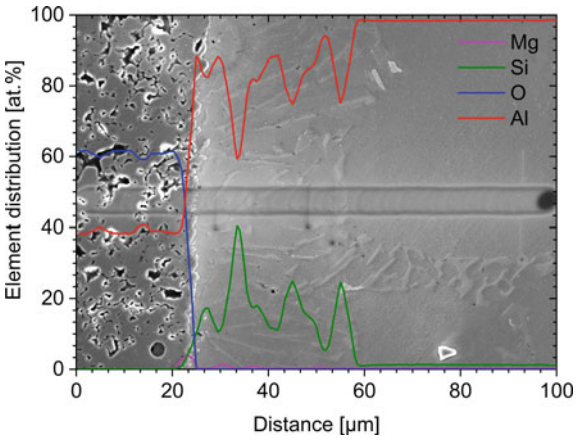

Fig. 7.14 SEM micrograph (Inlens/SE detector) of the alumina/aluminum alloy interface after 60 min at 750 °C, the contamination due to the EPMA line scan is visible, with corresponding EPMA line scan results (adopted from [3])

After a longer holding time (30 – 60 min), accumulation of Mg at the surface of the corundum filter was observed (Fig. 7.14). Although no distinct reaction layer was detected, the accumulation of Mg at the Al_2O_3/AlSi7Mg0.6 interface is regarded as a preliminary stage of the $MgAl_2O_4$ formation. Thermodynamic calculations supported this hypothesis and revealed that $MgAl_2O_4$ is the stable phase in the whole temperature range between 20 to 1000 °C [3]. According to the thermodynamic simulation, the formation of the $MgAl_2O_4$ spinel would, in the equilibrium state, fully consume the 0.6 mass% of Mg, which are available in AlSi7Mg0.6 [42, 43]. Consequently, no Mg-containing intermetallic phases, e.g., Mg_2Si (SG $Fm\bar{3}m$), should form. Silicon contained in the melt should precipitate upon cooling. These results of the thermodynamic simulation were proven experimentally. No Mg_2Si was found, while Si formed needles in the solidified melt (Fig. 7.14).

7.4.3 Reaction of AlSi7Mg0.6 with Amorphous SiO_2 and Mullite

It is known from literature [44–47] that aluminum silicates, e.g., mullite ($3Al_2O_3 \cdot 2SiO_2$), decompose in contact with molten aluminum, and form alumina and silica. Alumina usually crystallizes as corundum (α-Al_2O_3), while silica is reduced by liquid aluminum to silicon, which dissolves in the melt. This reaction results in additional formation of Al_2O_3 [44], which occurs in form of metastable alumina phases like η-, θ- and/or γ-Al_2O_3 [48–50]. The presence of Mg in the aluminum alloy is expected to alter the interfacial reactions and to produce additional phases like $MgAl_2O_4$ spinel and/or $MgSiO_3$ pyroxene.

Individual steps of the reaction between AlSi7Mg0.6 melt and SiO_2 or mullite were visualized by model experiments that were performed with compacted powder samples containing 50 mol% of the aluminum alloy and 50 mol% of SiO_2 or mullite.

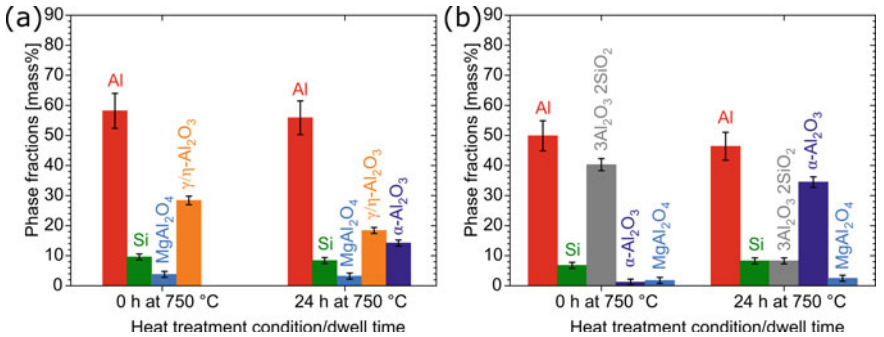

Fig. 7.15 **a** Phase composition of the powder mixture of AlSi7Mg0.6 and amorphous SiO_2 after heat treatment at 750 °C without dwell (0 h) and after 24 h at 750 °C (24 h). **b** Phase composition of the powder mixture of AlSi7Mg0.6 and mullite after heat treatment at 750 °C without dwell (0 h) and after 24 h at 750 °C (24 h) (adopted from [44])

A short-time reaction between molten AlSi7Mg0.6 alloy and amorphous SiO_2 at 750 °C led to the decomposition of SiO_2, and to the formation of Si, γ/η-Al_2O_3 and $MgAl_2O_4$ in the solidified sample (Fig. 7.15a, 0 h). Note that Fig. 7.15 includes only crystalline phases, because the phase fractions were determined using XRD. With longer reaction time (24 h at 750 °C), the amount of Al_2O_3 increases, and a part of metastable alumina (γ/η-Al_2O_3) transforms to corundum (α-Al_2O_3).

Reaction experiments, which were carried out with an alumina plate coated with amorphous SiO_2, revealed that Mg is attracted to the filter wall in the initial stages of the reaction process (Fig. 7.16a). However, as no magnesium silicate was found in the powder mixtures sintered for short time (Fig. 7.15a), it can be concluded that the functional SiO_2 coating dissolves rather than a magnesium silicate, e.g., $MgSiO_3$, forms. Free silicon forms Si precipitates, which were observed in the solidified AlSi7Mg0.6 melt (Fig. 7.16b). Oxygen reacts with Al and Mg to Al_2O_3 and to $MgAl_2O_4$ (Fig. 7.15a). In the planar sample, the coexistence of these compounds led to the formation of $MgAl_2O_4$ precipitates embedded in an Al_2O_3 layer (left part of Fig. 7.16b). The secondary Al_2O_3 layer is separated from the solidified melt by an Mg-rich and O-depleted interlayer (central part of Fig. 7.16b).

The reaction between molten AlSi7Mg0.6 and mullite leads to the formation of Si, Al_2O_3 and $MgAl_2O_4$ (Fig. 7.15b) as well. In this case, however, alumina exists in the thermodynamically stable form of corundum already in the initial stages of the reaction process. The formation of corundum instead of the metastable alumina phases is facilitated by the presence of α-Al_2O_3, which is a product of the mullite decomposition [44–47]. Figure 7.17 depicts the Si needles in the solidified AlSi7Mg0.6 melt and illustrates the preferential diffusion of Mg into the mullite coating along the pore and grain boundaries.

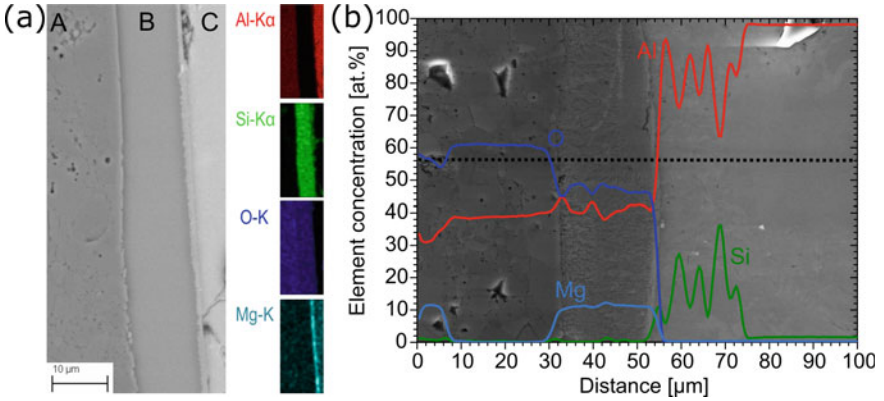

Fig. 7.16 **a** Left: SEM micrograph (BSE contrast) of the amorphous SiO_2 coating (B) on the Al_2O_3 substrate (A) after 1 min dwell at 750 °C in contact with the solidified AlSi7Mg0.6 alloy (C); Right: Results of EDX element mapping of the area on the left showing Mg enrichment on the interface SiO_2/alloy. **b** SEM micrograph (SE contrast) and overlaid EPMA line scan track (cross-centred black dashed line) with corresponding quantitative elemental analysis showing the α-Al_2O_3 substrate with an $MgAl_2O_4$ precipitate (left side) covered with a newly formed, Mg-enriched, Al- and O-containing and Si-free layer (middle) that replaces the SiO_2 coating after contact with the AlSi7Mg0.6 alloy (right side) at 750 °C for 30 min. The composite structure grows columnar-like (adopted from [44])

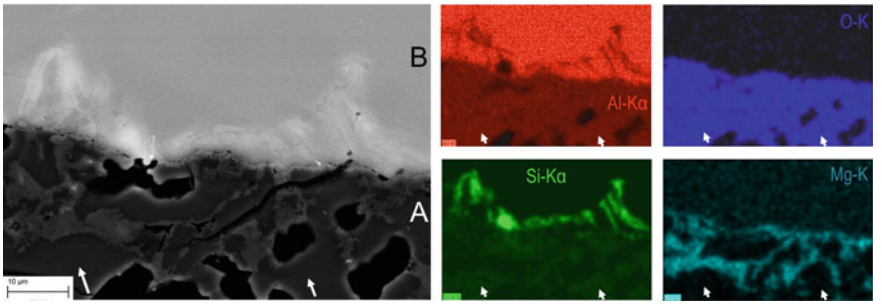

Fig. 7.17 Left: SEM micrograph (BSE contrast) of the mullite coating (**A**) after 30 min dwell at 750 °C in contact with the solidified AlSi7Mg0.6 alloy (**B**), pores and cracks (black) in the coating; Right: Results of EDX element mapping of the area on the left side showing Mg enrichment and Si depletion in the coating and silicon needles in the alloy. The centres of two large grains showing the stoichiometric composition of mullite ($3Al_2O_3{\cdot}2SiO_2$) are marked with white arrows (adopted from [44])

7.4.4 Reaction Between Al and AlSi7Mg0.6 Melts and TiO_2

In contact with molten Al or aluminum alloys, TiO_2 is reduced in analogy to SiO_2. Typical reaction products are Ti_3O_5, Ti_2O_3, TiO and Ti [12, 51–57]. Metallic Ti is dissolved in the melt. In our SPS experiments that were performed with the

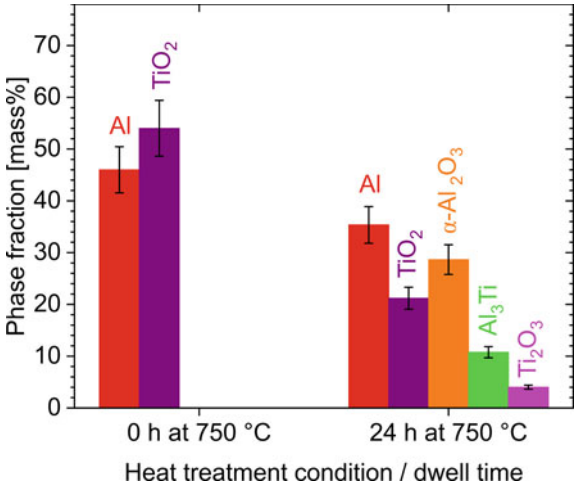

Fig. 7.18 Phase composition of the powder mixture of pure Al and TiO_2 after heat treatment at 750 °C without dwell (0 h) and after 24 h at 750 °C (24 h)

powder mixtures of Al and TiO_2 (rutile, SG $P4_2/mnm$), α-Al_2O_3 and Ti_2O_3 with the corundum crystal structures (SG $R\overline{3}c$) and Al_3Ti (SG *I4/mmm*) were found after 24 h at 750 °C (Fig. 7.18). In literature, also the formation of intermetallic phases like $(Al,Si)_3Ti$ (SG *I4/mmm*), $Al_{60}Si_{12}Ti_{28}$ or $Ti_7Al_5Si_{12}$ [12, 52, 55, 58, 59] was reported. Ti_2O_3 present in our samples is a product of the TiO_2 reduction. α-Al_2O_3 is a product of the reaction of Al with released oxygen. The formation of corundum (α-Al_2O_3) is possibly facilitated by the presence of Ti_2O_3 having the same crystal structure like α-Al_2O_3. Al_3Ti formed, because the Ti concentration in the melt exceeded locally the solubility limit for Ti in Al (< 1 at% at 750 °C).

The experiments carried out with planar samples disclosed that α-Al_2O_3 grows in form of a compact layer on the surface of the functional TiO_2 coating (Fig. 7.19). The analysis of the Al_2O_3/TiO_2 interface using SEM/EBSD revealed that Al_2O_3 grows on TiO_2 frequently with the orientation relationship $(001)_{TiO_2} \| (100)_{Al_2O_3}$ and $[010]_{TiO_2} \| [001]_{Al_2O_3}$ (Fig. 7.20). The round brackets stand for parallel lattice planes, the square brackets for parallel crystal axes. The slight misorientations (Fig. 7.20b) compensate the differences in the interatomic distances. The pronounced orientation relationship between α-Al_2O_3 and TiO_2 is a consequence of the similarity of their crystal structures (Fig. 7.20c, orientation relationships were plotted using VESTA 3 [60]) and of the possible presence of Ti_2O_3 as a thin interlayer. Such heteroepitaxial growth improves the adhesion of Al_2O_3 to TiO_2 significantly. Moreover, a compact corundum layer impedes the direct contact between molten aluminum and the TiO_2 coating, which inhibits a further reduction of rutile (and other titanium oxides) and the production of free titanium. The lack of reduced titanium retards or even hinders the formation of Al_3Ti.

In contact with molten AlSi7Mg0.6 alloy, TiO_2 forms quite quickly $MgTiO_3$ (SG $R\overline{3}$), cf. Fig. 7.21a. Additional oxygen, which is required for this reaction, is supplied by the melt. Silicon present in the AlSi7Mg0.6 melt forms Si precipitates.

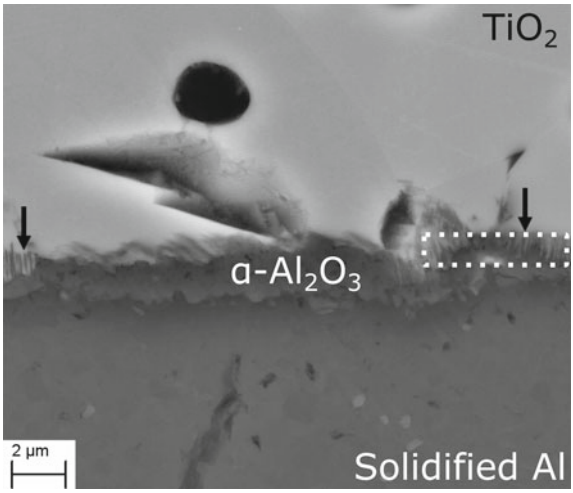

Fig. 7.19 SEM micrograph (BSE contrast) of the rutile coating brought in contact with molten Al at 750 °C for 300 min. The main reaction layer contains corundum (α-Al_2O_3). The white-dotted box shows the position of a FIB lamella, which was investigated by TEM and SAED (cf. Fig. 7.25) in order to explain the nature of the stripes marked by black arrows (adopted from [52])

The highly variable thickness of the $MgTiO_3$ layer (Fig. 7.21b) suggests that the diffusion of Mg and O into TiO_2 is accelerated, when the TiO_2 coating contains cracks, voids or grain boundaries. The analysis of the $MgTiO_3/TiO_2$ interface using SEM/EBSD revealed that the grains of magnesium titanate and rutile possess frequently an orientation relationship $(100)_{MgTiO_3} \| (001)_{TiO_2}$ and $[001]_{MgTiO_3} \| [010]_{TiO_2}$ (Fig. 7.22). Round brackets denote the lattice planes, while square brackets denote the crystal axes. This orientation relationship was confirmed by a local analysis of the $MgTiO_3/TiO_2$ interface using SAED in TEM (Fig. 7.23). The ab initio simulations using the density functional theory [52] revealed that the above orientation relationship reduces the total energy of the $MgTiO_3/TiO_2$ interface in comparison with the total energy of the individual bulk components.

Diffraction contrasts visible in the TEM micrograph (Fig. 7.23a) explained the slight misorientation between $MgTiO_3$ and TiO_2, which was first concluded from the results of the SEM/EBSD analysis (Fig. 7.22b). The diffraction contrasts stem from geometrically necessary misfit dislocations, which are distributed almost equidistantly along the $MgTiO_3/TiO_2$ interface and which compensate the lattice misfit between $MgTiO_3$ and TiO_2. These dislocations produce small angle grain boundaries that are visible by SEM/EBSD as slight departures from the ideal orientation relationship.

Furthermore, the local analysis of the reaction zone between TiO_2 and the solidified AlSi7Mg0.6 melt using TEM and SAED contributed essentially to the understanding of the reaction kinetics in this system. Within the original TiO_2 coating, bands of Ti_2O_3 (SG $R\bar{3}c$, corundum type) and $MgTiO_3$ (SG $R\bar{3}$) having

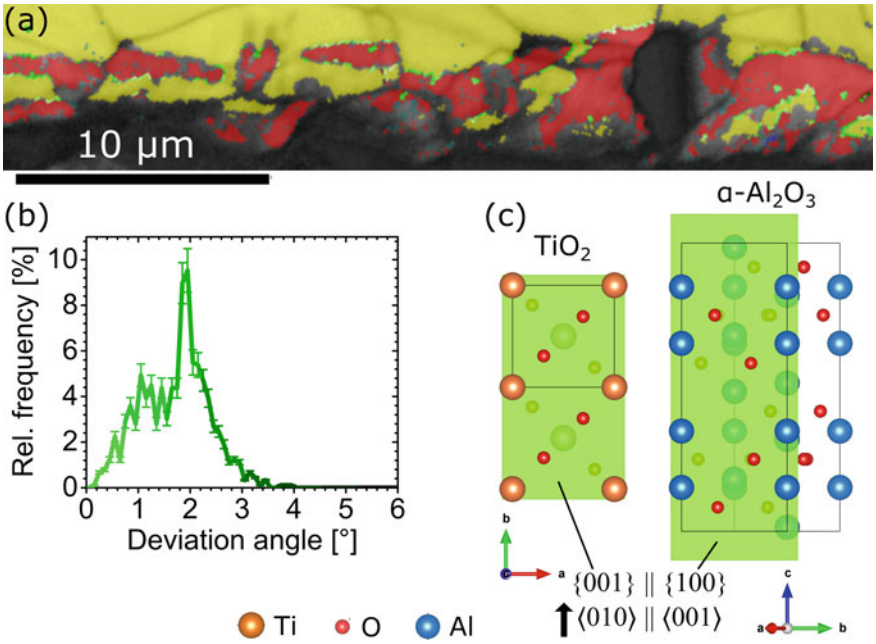

Fig. 7.20 **a** EBSD phase map of the TiO_2/Al interface after 60 min at 750 °C. Rutile is plotted in yellow, corundum in red. Black areas within the colorized region are pores, non-indexed bottom region is solidified aluminum. The green lines mark the interfaces between rutile and corundum crystallites having the orientation relationship $(001)_{TiO_2} \| (100)_{Al_2O_3}$ and $[010]_{TiO_2} \| [001]_{Al_2O_3}$. A histogram of the local deviations from this orientation relationship is shown in (**b**). **c** Model of rutile and corundum in the above orientation relationship plotted using VESTA 3 [60] (adopted from [52])

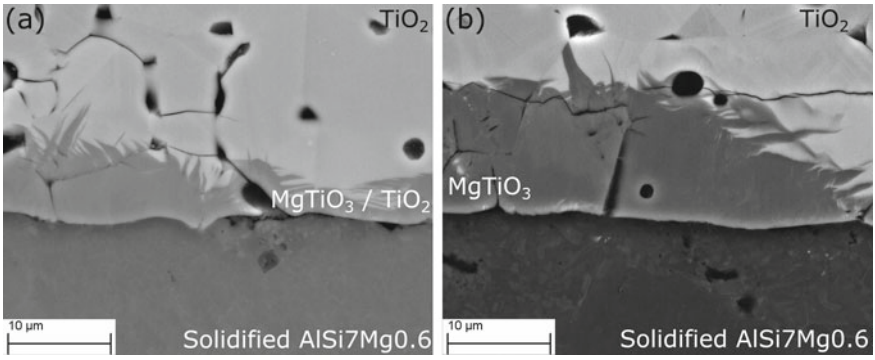

Fig. 7.21 SEM micrographs (BSE contrast) of the rutile coating brought in contact with molten AlSi7Mg0.6 alloy for 60 min (**a**) and 300 min (**b**) at 750 °C. At the interface between the coating and the liquid alloy, a $MgTiO_3$ layer formed (adopted from [52])

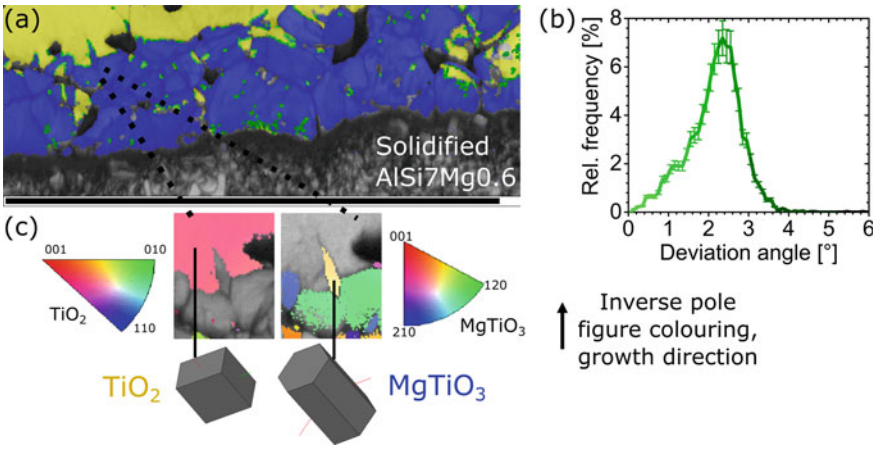

Fig. 7.22 Results of the EBSD analysis performed on the rutile coating after 60 min at 750 °C. **a** Phase map showing the distribution of rutile (yellow) and $MgTiO_3$ (blue). Pores/voids are reproduced in black, the grey region at the bottom is the solidified alloy AlSi7Mg0.6. The green lines mark the interfaces between the TiO_2 and $MgTiO_3$ grains having the orientation relationship $(100)_{MgTiO_3} \| (001)_{TiO_2}$ and $[001]_{MgTiO_3} \| [010]_{TiO_2}$. A histogram of the local deviations from this orientation relationship is shown in (**b**). The above orientation relationship is illustrated in figure (c) (adopted from [52])

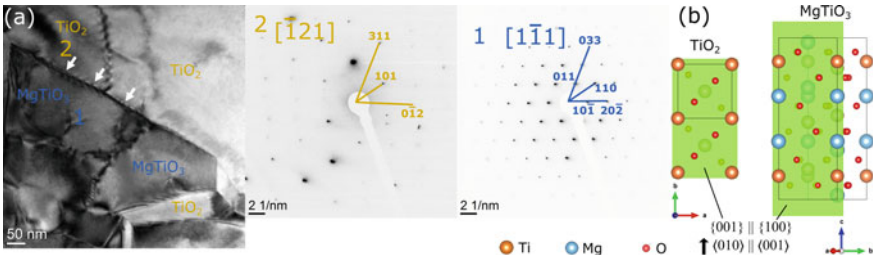

Fig. 7.23 **a** A TEM micrograph of the $MgTiO_3/TiO_2$ interface after 60 min at 750 °C. A phase boundary with geometrically necessary misfit dislocations is marked by white arrows. The orientation relationship $(100)_{MgTiO_3} \| (001)_{TiO_2}$ and $[001]_{MgTiO_3} \| [010]_{TiO_2}$ shown in panel **b** was verified by SAED. Crystal structures were created with the VESTA 3 software [60] (adopted from [52])

a pronounced heteroepitaxial orientation relationship $(001)_{Ti_2O_3} \| (001)_{MgTiO_3}$ and $[100]_{Ti_2O_3} \| [100]_{MgTiO_3}$ at their interfaces were detected (Fig. 7.24). The thickness of the individual stripes was about 200 nm. The formation of such structures is facilitated by a local oxygen deficiency. When a sufficient amount of magnesium but a low amount of oxygen diffuse into the TiO_2 coating, the oxygen that is required for the formation of $MgTiO_3$ is produced by the reduction of TiO_2, which leads to the formation of Ti_2O_3. Note that Ti_2O_3 and $MgTiO_3$ are miscible in a broad range of the Ti and Mg concentrations [61] and that $MgTiO_3$ belongs to the group of ilmenites, which can accommodate various metallic species in their crystal structure,

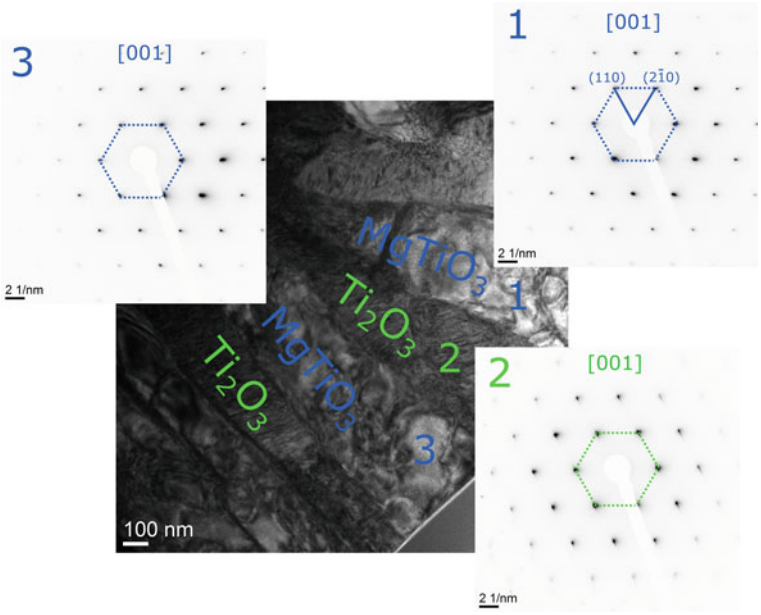

Fig. 7.24 TEM and SAED of the $MgTiO_3/Ti_2O_3$ interfaces of the TiO_2 coating that was in contact with the AlSi7Mg0.6 melt for 300 min at 750 °C. The growth direction is perpendicular to the plane of the image (adopted from [52])

e.g., Fe and Mn in addition to or instead of Mg and Ti [62]. Thus, the $MgTiO_3/Ti_2O_3$ composite layer can incorporate a variety of alloying or foreign elements.

When TiO_2, Mg and O come into contact with alumina, e.g., near the interface between the Al_2O_3 filter wall and the functional rutile coating, $MgAl_2O_4$ spinel forms as an additional phase (Fig. 7.25). Whereas the titanium magnesium oxides exist in the form of ilmenite ($MgTiO_3$, SG$R\bar{3}$) and spinel ($Mg(Ti_{1-x}Mg_x)O_4$, SG$Fd\bar{3}m$) [63], $MgAl_2O_4$ exists only in the spinel form. Furthermore, $Mg(Ti_{1-x}Mg_x)O_4$ and $MgAl_2O_4$ are not miscible. Therefore, a complex microstructure consisting of the TiO_2, $MgTiO_3$ and $MgAl_2O_4$ phases with segregated Ti and Al atoms forms in the reaction zone containing Ti, Mg, O and Al (Fig. 7.25). Nevertheless, the SAED patterns (Fig. 7.25) indicated that these phases possess a pronounced orientation relationship, which was described as $(100)_{TiO_2} \| \left(11\bar{1}\right)_{MgAl_2O_4} \| (001)_{MgTiO_3}$ and $[001]_{TiO_2} \| [011]_{MgAl_2O_4} \| [120]_{MgTiO_3}$ and which is substantiated by the crystal structure models depicted in Fig. 7.26. Also in this case, the heteroepitaxy of the neighboring phases is believed to improve the adhesion of the reaction layers formed during the filtration process.

The layer formation in each case provided evidence for the "reactive" interaction between metal melt and the functional filter ceramic coating, i.e. rutile, consuming magnesium and dissolved detrimental oxygen.

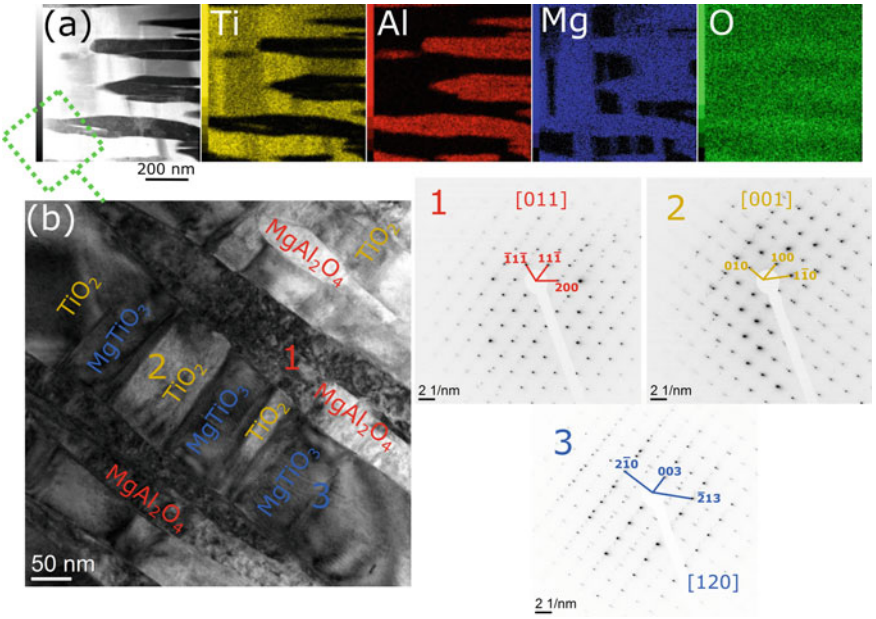

Fig. 7.25 Element maps (**a**) and TEM micrograph (**b**) of the stripes from Fig. 7.19. Individual phases were assigned using a combination of chemical analysis (EDX) and SAED. The viewing direction is perpendicular to the sample surface and corresponds to the growth direction of corundum into rutile (adopted from [52])

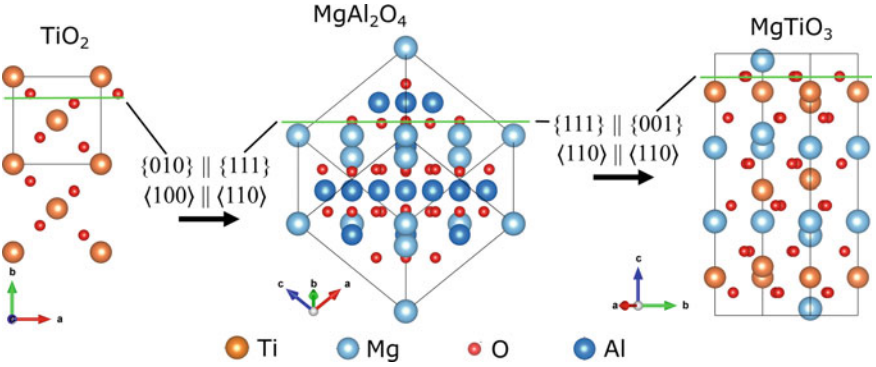

Fig. 7.26 Crystal structure models of TiO_2, $MgAl_2O_4$ and $MgTiO_3$ mutually oriented according to the orientation relationships that were identified using SAED (cf. Fig. 7.25). The parallel planes highlighted in green mark close-packed oxygen sublattice planes in each structure (highly distorted in rutile), arrows mark the corresponding parallel directions. The crystal structures were created with VESTA 3 [60] (adopted from [52])

The binding mechanism between the newly formed magnesium titanate layer and rutile was also investigated systematically to make sure that no spalling or peel-off of $MgTiO_3$ could contaminate the filtered alloy melt. The $MgTiO_3$ layer growth at the interface between the AlSi7Mg0.6 melt and rutile depends strongly on the local orientation of the TiO_2 grains.

7.5 Summary and Conclusions

In this contribution, the reaction processes between functionalized metal melt filters and molten 42CrMo4 steel, pure aluminum melt and molten AlSi7Mg0.6 alloy were studied. The samples were produced in a Spark Plasma Sintering apparatus with modified tooling. This experimental setup allowed very fast heating of the samples, controlled melting of the metals and the investigation of reaction processes at constant reaction temperatures and without convection of the melt.

The initial products of the reaction between molten 42CrMo4 steel and carbon-bonded corundum (Al_2O_3-C) filters were dissolved aluminum and oxygen, CO/CO_2 gas and an amorphous reaction layer, which contained Fe, Al, O as well as the alloying elements and impurities from the steel. After a longer reaction time, nanocrystalline wuestite, garnets, spinel-like phases including metastable alumina, and secondary corundum formed. The production of CO/CO_2, the formation of reaction layers and the growth of secondary corundum contributed significantly to the reduction of the oxygen content in the steel melt. When the secondary corundum grows directly on the primary corundum from the metal melt filter, the growth is epitaxial. The habitus of the secondary corundum (attached platelets or compact layers) depends on the local availability of carbon in the reaction zone, on the carbon concentration in the Al_2O_3-C filter and on the filter morphology.

When the carbon-bonded corundum is coated with carbon-bonded magnesium oxide, $MgAl_2O_4$ spinel forms in a carbothermic reaction between corundum from the Al_2O_3-C substrate and MgO. This reaction is facilitated by the presence of iron from the molten 42CrMo4 steel. Iron that penetrates into the porous MgO-C coating promote the formation of $MgAl_2O_4$ whiskers at the interface between the MgO-C coating and the Al_2O_3-C substrate. These whiskers are supposed to strengthen the filter ceramics, which is an additional benefit to the removal of oxygen from the melt, to the increased flotation of oxygen and inclusions present in the melt by the CO/CO_2 bubbles and to growth of secondary $MgAl_2O_4$ as docking sites for further deposition of endogenous inclusions.

In contact with molten aluminum, functional coatings made from corundum stay intact. Still, they serve as substrate for secondary corundum, which forms from aluminum and oxygen dissolved in the melt. In contrast to Al_2O_3, SiO_2 dissolves completely. Reduced silicon is solved in the melt. Free oxygen reacts with Al to metastable alumina (γ/η-Al_2O_3), which transforms later to corundum (α-Al_2O_3). Mullite ($3Al_2O_3 \cdot 2SiO_2$) decomposes to α-Al_2O_3 and SiO_2. SiO_2 dissolves quickly; α-Al_2O_3 serves as substrate for secondary corundum. Consequently, no metastable

alumina phases are formed, when mullite is brought in contact with molten Al. In functional coatings made from rutile, TiO_2 is reduced by molten Al to Ti_2O_3. Free oxygen (including the original oxygen present in the melt) reacts with Al to corundum.

The reactions between molten AlSi7Mg0.6 alloy and the functional coatings made from corundum, mullite and SiO_2 are accompanied by the formation of $MgAl_2O_4$, which is a product of the reaction of Mg and O with Al_2O_3. The other reactions and processes are the same like for the Al melt. Mullite decomposes into corundum and SiO_2. SiO_2 dissolves. Reduced Si is solved in the melt. Oxygen reacts with Al and Mg to Al_2O_3 and $MgAl_2O_4$. On the surface of the corundum and mullite filters, where corundum is present (in mullite as a product of the $3Al_2O_3 \cdot 2SiO_2$ decomposition), Al_2O_3 crystallizes as corundum. If Al_2O_3 cannot grow directly on corundum substrate, e.g., on the surface of a SiO_2 coating, metastable alumina phases are formed first. The TiO_2 coatings react with Mg and O from the melt to $MgTiO_3$. If the local concentration of Mg is higher than the local concentration of O, TiO_2 is reduced to Ti_2O_3. When $MgTiO_3$ comes in contact with Al_2O_3 that stems, e.g., from the skeleton of the filter, $MgAl_2O_4$ and TiO_2 or Ti_2O_3 are formed.

Our study illustrated the importance of the spinel-like structures, which were found in all filter/melt combinations under consideration. In all cases, the spinel-like phases (in particular $MgAl_2O_4$) accommodated oxygen and impurities from the melts. Furthermore, the spinel-like phases are expected to dock the inclusions having the spinel structure, e.g., the metastable alumina phases. For these reasons, the spinel-like phases are considered as possible candidates for production of the functional coatings covering the metal melt filters.

Another finding of this study concerns the role of the epitaxial or heteroepitaxial growth of secondary coatings during the filtration process. Although many of the (primary) functional coatings under study decomposed in contact with the metal melt, the solved elements were captured in oxides, which formed in a secondary "deposition" process. It was shown that almost all oxides involved in this process are able to grow by mutual heteroepitaxy. This was proven for Al_2O_3, Ti_2O_3 (both having the corundum structure), TiO_2 (rutile), $MgAl_2O_4$ (spinel) and $MgTiO_3$ (ilmenite).

Acknowledgements The former CRC 920 project collaborators are highly acknowledged for their contributions: Milan Dopita, Tilo Zienert, Lilit Amirkhanyan, Marcus Emmel, Claudia Voigt, Eva Jäckel and Anne Schmidt. Furthermore, we thank Christiane Ullrich, Steffen Dudczig, Jana Hubalkova, Brigitte Bleiber, Dietrich Heger, Beate Kutzner, Christian Schimpf, Diane Hübgen, Katrin Becker, Astrid Leuteritz, Karin Müller and Galina Savinykh for their support with production, preparation and analysis of the samples. The electron probe microanalyzer was funded by the German Research Foundation in the frame of the Major Research Instrumentation Program under the project number 395240765. The German Research Foundation (DFG) is acknowledged for funding the Collaborative Research Centre 920—Project-ID 169148856, subproject A06.

References

1. C. Voigt, T. Zienert, P. Schubert, C.G. Aneziris, J. Hubalkova, J. Am. Ceram. Soc. **97**, 2046 (2014). https://doi.org/10.1111/jace.12977
2. C. Voigt, E. Jäckel, C.G. Aneziris, J. Hubalkova, Ceram. Int. **39**, 2415 (2013). https://doi.org/10.1016/j.ceramint.2012.09.001
3. A. Salomon, T. Zienert, C. Voigt, E. Jäckel, O. Fabrichnaya, D. Rafaja, C.G. Aneziris, Adv. Eng. Mat. **15**, 1206 (2013). https://doi.org/10.1002/adem.201300114
4. S. Dudczig, C.G. Aneziris, M. Emmel, G. Schmidt, J. Hubalkova, H. Berek, Ceram. Int. **40**, 16727 (2014). https://doi.org/10.1016/j.ceramint.2014.08.038
5. C. Voigt, E. Jäckel, F. Taina, T. Zienert, A. Salomon, G. Wolf, C.G. Aneziris, P. Le Brun, Metall. Mater. Trans. B **48**, 497 (2016). https://doi.org/10.1007/s11663-016-0869-5
6. M. Emmel, C.G. Aneziris, F. Sponza, S. Dudczig, P. Colombo, Ceram. Int. **40**, 13507 (2014). https://doi.org/10.1016/j.ceramint.2014.05.033
7. M. Emmel, C.G. Aneziris, J. Mater. Res. **28**, 2234 (2013). https://doi.org/10.1557/jmr.2013.56
8. M. Emmel, C.G. Aneziris, Ceram. Int. **38**, 5165 (2012). https://doi.org/10.1016/j.ceramint.2012.03.022
9. O. Guillon, J. Gonzalez-Julian, B. Dargatz, T. Kessel, G. Schierning, J. Räthel, M. Herrmann, Adv. Eng. Mat. **16**, 830 (2014). https://doi.org/10.1002/adem.201300409
10. H.U. Kessel, J. Hennicke, Interceram **56**, 164 (2007)
11. A. Salomon, M. Emmel, S. Dudczig, D. Rafaja, C.G. Aneziris, Adv. Eng. Mat. **15**, 1235 (2013). https://doi.org/10.1002/adem.201300119
12. A. Salomon, C. Voigt, O. Fabrichnaya, C.G. Aneziris, D. Rafaja, Adv. Eng. Mat. **19**, 1700106 (2017). https://doi.org/10.1002/adem.201700106
13. A. Schmidt, A. Salomon, S. Dudczig, H. Berek, D. Rafaja, C.G. Aneziris, Adv. Eng. Mat. **19**, 1700170 (2017). https://doi.org/10.1002/adem.201700170
14. C.G. Aneziris, S. Dudczig, M. Emmel, H. Berek, G. Schmidt, J. Hubalkova, Adv. Eng. Mat. **15**, 46 (2013). https://doi.org/10.1002/adem.201200199
15. H.M. Rietveld, Acta Crystallogr. **22**, 151 (1967). https://doi.org/10.1107/S0365110X67000234
16. H.M. Rietveld, J. Appl. Crystallogr. **2**, 65 (1969). https://doi.org/10.1107/S0021889869006558
17. L. Lutteroti, S. Matthies, H.R. Wenk, CPD Newsletter (IUCr) May 1999, 21. http://www.mx.iucr.org/iucr-top/comm/cpd/Newsletters/no21may1999/art17/art17.htm
18. S.N. Singh, Metall. Trans **5**, 2165 (1974). https://doi.org/10.1007/BF02643930
19. A.S. Kondrat'ev, V.N. Popov, L.M. Aksel'rod, M.R. Baranovskii, S.A. Suvorov, N.B. Tebuev, Refractories 31, 384 (1991). https://doi.org/10.1007/BF01281545
20. R. Dekkers, B. Blanpain, P. Wollants, F. Haers, C. Vercruyssen, B. Gommers, Ironmak. Steelmak. **29**, 437 (2002). https://doi.org/10.1179/030192302225004584
21. J. Poirier, Metall. Res. Technol. **112**, 410 (2015). https://doi.org/10.1051/metal/2015028
22. M. Emmel, C.G. Aneziris, G. Schmidt, D. Krewerth, H. Biermann, Adv. Eng. Mat. **15**, 1188 (2013). https://doi.org/10.1002/adem.201300118
23. X. Wu, Y. Ranglack-Klemm, J. Hubálková, J. Solarek, C.G. Aneziris, A. Weidner, H. Biermann, Ceram. Int. **47**, 3920 (2020). https://doi.org/10.1016/j.ceramint.2020.09.255
24. J. Solarek, C. Himcinschi, Y. Klemm, C.G. Aneziris, H. Biermann, Carbon **122**, 141 (2017). https://doi.org/10.1016/j.carbon.2017.06.041
25. H. Zielke, T. Wetzig, C. Himcinschi, M. Abendroth, M. Kuna, C.G. Aneziris, Carbon **159**, 324 (2020). https://doi.org/10.1016/j.carbon.2019.12.042
26. M. Neumann, T. Wetzig, J. Fruhstorfer, V. Lampert, H. Jelitto, G.A. Schneider, C.G. Aneziris, Ceram. Int. **46**, 11198 (2020). https://doi.org/10.1016/j.ceramint.2020.01.141
27. T. Zienert, S. Dudczig, O. Fabrichnaya, C.G. Aneziris, Ceram. Int. **41**, 2089 (2015). https://doi.org/10.1016/j.ceramint.2014.10.004
28. R. Khanna, S. Kongkarat, S. Seetharaman, V. Sahajwalla, ISIJ Int. **52**, 992 (2012). https://doi.org/10.2355/isijinternational.52.992
29. A. Salomon, M. Motylenko, D. Rafaja, Adv. Eng. Mat. **24**, 2100690 (2021). https://doi.org/10.1002/adem.202100690

30. C.E. Sims, F.B. Dahle, Trans. Am. Foundrymen's Assoc. **46**, 65 (1938)
31. H. Ohta, H. Suito, ISIJ Int. **46**, 480 (2006). https://doi.org/10.2355/isijinternational.46.480
32. S. Henschel, J. Gleinig, T. Lippmann, S. Dudczig, C.G. Aneziris, H. Biermann, L. Krüger, A. Weidner, Adv. Eng. Mat. **19**, 1700199 (2017). https://doi.org/10.1002/adem.201700199
33. M. Rudolph, M. Motylenko, D. Rafaja, IUCrJ **6**, 116 (2019). https://doi.org/10.1107/S2052252518015786
34. M.-A. Faghihi-Sani, A. Yamaguchi, Ceram. Int. **28**, 835 (2002). https://doi.org/10.1016/S0272-8842(02)00049-4
35. M. Bavand-Vandchali, F. Golestani-Fard, H. Sarpoolaky, H.R. Rezaie, C.G. Aneziris, J. Eur. Cer. Soc. **28**, 563 (2008). https://doi.org/10.1016/j.jeurceramsoc.2007.07.009
36. M. Ahmadi Najafabadi, M. Hirasawa, M. Sano, ISIJ Int. **36**, 1366 (1996). https://doi.org/10.2355/isijinternational.36.1366
37. A. Salomon, M. Dopita, M. Emmel, S. Dudczig, C.G. Aneziris, D. Rafaja, J. Eur. Cer. Soc. **35**, 795 (2015). https://doi.org/10.1016/j.jeurceramsoc.2014.09.033
38. V. Brabie, Steel Res. **68**, 54 (1997). https://doi.org/10.1002/srin.199700542
39. S. Jansson, V. Brabie, P. Jönsson, Ironmak. Steelmak. **33**, 389 (2006). https://doi.org/10.1179/174328106X113977
40. Z. Xie, F. Ye, J. Wuhan Univ. Technol. Mat. Sci. Ed. **24**, 896 (2009). https://doi.org/10.1007/s11595-009-6896-1
41. C. Voigt, L. Ditscherlein, E. Werzner, T. Zienert, R. Nowak, U. Peuker, N. Sobczak, C.G. Aneziris, Mater. Design **150**, 75 (2018). https://doi.org/10.1016/j.matdes.2018.04.026
42. T. Zienert, O. Fabrichnaya, Adv. Eng. Mat. **15**, 1244 (2013). https://doi.org/10.1002/adem.201300113
43. L. Dreval, T. Zienert, O. Fabrichnaya, J. Alloys Compds. **657**, 192 (2016). https://doi.org/10.1016/j.jallcom.2015.10.017
44. A. Salomon, T. Zienert, C. Voigt, M. Dopita, O. Fabrichnaya, C.G. Aneziris, D. Rafaja, Corros. Sci. **114**, 79 (2017). https://doi.org/10.1016/j.corsci.2016.10.023
45. K.J. Brondyke, J. Am. Ceram. Soc. **36**, 171 (1953). https://doi.org/10.1111/j.1151-2916.1953.tb12860.x
46. S. Afshar, C. Allaire, JOM **48**, 23 (1996). https://doi.org/10.1007/BF03222938
47. A.L. Yurkov, I.A. Pikhutin, Refract. Ind. Ceram. **50**, 212 (2009). https://doi.org/10.1007/s11148-009-9184-x
48. A.E. Standage, M.S. Gani, J. Am. Ceram. Soc. **50**, 101 (1967). https://doi.org/10.1111/j.1151-2916.1967.tb15049.x
49. C. Marumo, J.A. Pask, J. Mater. Sci. **12**, 223 (1977). https://doi.org/10.1007/BF00566262
50. P. Mossino, D. Vallauri, F.A. Deorsola, L. Pederiva, R. Dal Maschio, G. Scavino, I. Amato, Metallurgia Italiana **97**, 25 (2005)
51. M. Ilatovskaia, G. Savinykh, O. Fabrichnaya, J. Phase Equ. Diff. **38**, 175 (2017). https://doi.org/10.1007/s11669-016-0509-4
52. A. Salomon, L. Amirkhanyan, C. Ullrich, M. Motylenko, O. Fabrichnaya, J. Kortus, D. Rafaja, J. Eur. Cer. Soc. **38**, 5590 (2018). https://doi.org/10.1016/j.jeurceramsoc.2018.07.052
53. I. Gheorghe, H.J. Rack, Mater. Sci. Technol. **18**, 1079 (2002). https://doi.org/10.1179/026708302225005990
54. P. Shen, H. Fujii, K. Nogi, Acta Mater. **54**, 1559 (2006). https://doi.org/10.1016/j.actamat.2005.11.024
55. S. Avraham, P. Beyer, R. Janssen, N. Claussen, W.D. Kaplan, J. Eur. Cer. Soc. **26**, 2719 (2006). https://doi.org/10.1016/j.jeurceramsoc.2005.06.024
56. J. Pan, J.H. Li, H. Fukunaga, X.G. Ning, H.Q. Ye, Z.K. Yao, D.M. Yang, Compos. Sci. Technol. **57**, 319 (1997). https://doi.org/10.1016/S0266-3538(96)00127-3
57. Z.-C. Chen, T. Takeda, K. Ikeda, Compos. Sci. Technol. **68**, 2245 (2008). https://doi.org/10.1016/j.compscitech.2008.04.006
58. I. Tsuchitori, N. Morinaga, H. Fukunaga, J. Jpn. I. Met. **59**, 331 (1995). https://doi.org/10.2320/jinstmet1952.59.3_331

59. S. Avraham, W.D. Kaplan, J. Mater. Sci. **40**, 1093 (2005). https://doi.org/10.1007/s10853-005-6922-4
60. K. Momma, F. Izumi, J. Appl. Crystallogr. **44**, 1272 (2011). https://doi.org/10.1107/S0021889811038970
61. A.B. Sheikh, J.T.S. Irvine, J. Solid State Chem. **103**, 30 (1993). https://doi.org/10.1006/jssc.1993.1075
62. C. Klein, C.S. Hurlbut, Jr., Manual of mineralogy (after James D. Dana), 21st ed., (New York: Wiley, 1993), pp. 380–381, ISBN 047157452X
63. B.A. Wechsler, R.B. von Dreele, Acta Cryst. B **45**, 542 (1989). https://doi.org/10.1107/S01087681890078 6X